Materials Today Bio 15 (2022) 100317

Contents lists available at ScienceDirect

Materials Today Bio

journal homepage: www.journals.elsevier.com/materials-today-bio

Imaging of fluorescent polymer dots in relation to channels and immune cells in the lymphatic system

Yufan Zhang, Juxiang Zhang, Xiaowei Li, Jingru Li, Shuting Lu, Yuqiao Li, Panting Ren, Chunfu Zhang, Liqin Xiong *

Shanghai Med-X Engineering Center for Medical Equipment and Technology, School of Biomedical Engineering, Shanghai Jiao Tong University, Shanghai, 200030, PR China

ARTICLE INFO

Keywords:
Polymer dots
Lymphatic system
Immune cells
Lymphatic vessels
Collagen fibers

ABSTRACT

Polymer dots (Pdots) have been applied to imaging lymph nodes (LNs) and lymphatic vessels (LVs) in living mice and rats. However, the mechanism of absorption, distribution, metabolism, and excretion of Pdots in LNs and LVs is still unclear. Therefore, the relationship between Pdots and immune cells, LVs and collagen fibers in lymphatics was studied by multiple *in vivo* and *ex vivo* microscopic imaging methods and detection techniques. Flow cytometry showed that Pdots could be phagocytosed by macrophages and monocytes, and had no relationship with B cells, T cells and dendric cells in LNs. Silver staining, immunofluorescence and two-photon microscope showed that Pdots gathered in collagen fibers and LVs of LNs. Furthermore, immunofluorescence imaging results verified that Pdots were distributed in the extracellular space of collecting LVs endothelial cells. In addition, Pdots in the collecting LVs were basically cleared by leaking into the surrounding tissue or draining LNs after 21 days of injection. During the long-time observation, Pdots also helped monitor the contraction frequency and variation range of LV. Our study lays a foundation on the research of Pdots as the carrier to study lymphatic structure and function in the future.

1. Introduction

The mammalian circulatory system includes the cardiovascular system and the lymphatic system. Unlike the closed, high-pressure and circulating vascular system, the lymphatic system forms an open, low-pressure and one-way transport network from the extracellular space to the venous system [1]. The lymphatic system reflects a complex network of lymphatic vessels (LVs), lymph nodes (LNs) and lymphatic organs [2]. The system is responsible for maintaining tissue fluid balance, and serves as a conduit for immune cell transportation and dietary fat uptake in the intestine [1,3–6]. This fascinating vasculature is now thought to be dynamically and actively involved in health and disease [7–9].

LVs are essential for the transportation of leukocytes and soluble antigens from peripheral tissues to the draining LNs [1]. It is lined with lymphatic endothelial cells (LECs) and have a thin layer of smooth muscle and outer membrane that bind LVs to surrounding tissues. In general, LVs are difficult to see because they contain few cells and carry mostly clear lymph. Thus, most visualization techniques rely on the natural ability of LVs to absorb tracers that are injected into tissue space [3,10]. Indocyanine green (ICG) - lymphangiography has become an essential diagnostic test for assessing the lymphatic system [11]. However, due to the leakage of small molecular dyes, it is urgent to find a convenient way with a photostable probe to monitor the change of LVs. Furthermore, lymphatic structures such as LNs are distributed along the LV network. LN reticular network limits lymphatic transportation of solutes into cortical parenchyma [12]. In fact, through LN drainage, the lymphatic system ensures that pathogens invading tissues are not directed into the bloodstream, but are captured by macrophages and dendric cells (DCs) present in LNs [1,13–15]. Therefore, it is important to image the reaction process in LNs due to the immune response.

Lymphatic system is not only the drainage system of systemic circulation, but also closely related to inflammation, cancer, organ transplantation and autoimmune diseases. Therefore, it is of great significance to study the lymphatic system. For a growing number of clinical indications, widespread used imaging techniques should be improved in order to meet the demand of evaluating the lymphatic system in patients and preclinical disease models clearly [2,14,16,17]. Modified polymer dots (Pdots) are employed as the fluorescent nanoprobe due to their

* Corresponding author.
E-mail address: xiongliqin@sjtu.edu.cn (L. Xiong).

https://doi.org/10.1016/j.mtbio.2022.100317
Received 12 March 2022; Received in revised form 21 May 2022; Accepted 5 June 2022
Available online 12 June 2022

excellent chemical and optical properties such as high fluorescence intensity, good photostability, excellent biocompatibility and low toxicity [18–23]. And Pdots have been used for *in vivo* imaging of lymphatics in blank and tumor mice [19–21]. However, the mechanism of Pdots imaging lymphatic system is still unclear. In this article, we made research on the relationship between Pdots and immune cells, LVs and collagen fibers in lymphatics. The results showed that Pdots could observe the structure change of LV over a period of time including contractility, lymphatic valves, and branches. Flow cytometer and two-photon microscope (TPM) showed the entered Pdots in the LNs had the close relevancy with macrophages in different sites and monocytes due to the ability of removing foreign bodies. Additionally, Pdots flowed in channels as LVs and collagen fibers that provided the zone for DCs to capture antigens. Our study lays a foundation on the research of Pdots as the carrier to study lymphatic structure and LN therapy in the future.

2. Materials and methods

2.1. Materials

Unless otherwise stated, all chemicals and solvents were of analytical grade and used without further purification. Benzyl alcohol, *tert*-butanol, benzyl benzoate and Poly(9,9-dioctylfluorene-altbenzothiadiazole) (PFBT, average $M_n \leq 25000$) were purchased from Sigma-Aldrich, Inc. Poly(9,9-dioctylfluorene-altbenzothiadiazole) (PFBT, average M_w = 19000) were obtained from American Dye Source, Inc. Poly[(9,9-dioctylfluorenyl-2,7-diyl)-co -(1,4-benzo-{2,1',3}-thiadiazole)]-*End-capped with DMP* (PFBT, average $M_w = 47000$) were bought from American Dye Source, Inc. Diphenyl ether (DPE) and vitamin E were commercially available from Alfa Aesar Co., Ltd. The Polystyrene Graft Ethylene Oxide functionalized with carboxylic end group (PS-PEG-COOH) and amino-terminated poly(methyl methacrylate) (PMMA-NH_2) were purchased from Polymer Source Inc.

2.2. Synthesis of polymer dots (Pdots)

The synthesis method was similar to that in previous articles [18–21, 23]. In brief, prepared ingredients such as three molecular weights of PFBT (average M_w = 19000, average $M_n \leq 25000$ and average M_w = 47000), PS-PEG-COOH and MMA-NH_2 were dissolved in THF (J&K). Then, the combinations of different original solutions synthesized different **Pdots** in Table S1. The combination of PFBT (average M_w = 19000) with PS-PEG-COOH as Pdots is called for **1.9 PC**. The combination of PFBT (average $M_n \leq 25000$) with PS-PEG-COOH as Pdots is called for **2.5 PC**. The combination of PFBT (average $M_n \leq 25000$) with PMMA-NH_2 as Pdots is called for **2.5 PN**. The combination of PFBT (average $M_w = 47000$) with PS-PEG-COOH as Pdots is called for **4.7 PC**. The combination of PFBT (average M_w = 47000) with PMMA-NH_2 as Pdots is called for **4.7 PN**. Unless mentioned, all the solution injected into LNs were concentrated ten times.

2.3. Characterization of Pdots

The hydrodynamic size and Zeta potential of different Pdots were measured with a Malvern Zetasizer Nano ZSP instrument (Malvern, UK) (DLS). The normalized UV–vis absorption spectra were measured via a Shimadzu UV-2550 ultraviolet–vis spectrometer (Shimadzu, China). The fluorescence emission spectra were collected using a HITACHI F-2700 fluorescence spectrophotometer.

2.4. Preparation of uDISCO solutions

The traditional preparing procedure of uDISCO solution for high-resolution 3D imaging has been mentioned before [24]. Firstly, *tert*-butanol solutions with distilled water mixed as 30 vol%, 50 vol%, 70 vol%, 80 vol%, 90 vol% and 96 vol% for gradient dehydration solution. Then, BABB was obtained with benzyl alcohol and benzyl benzoate as the volume of 1:2. BABB-D4 was prepared by mixing BABB with DPE at a ratio of 4:1 (vol/vol). In the end, 0.4% Vol vitamin E was added into BABB-D4 solutions to scavenge the peroxides.

2.5. In vitro collagen hydrogel penetration of Pdots

The concentration of collagen hydrogels was prepared at 7.38mg/mL as reported before [12]. Briefly, rat tail collagen (8.6 mg/mL, 142 μL, 354249, Corning, USA), EDTA (0.17 M, 19.5 μL) and NaOH (1 M, 3.8 μL) were mixed. The mixture solution was drawn into capillary tubes (Inner diameter 300 μm, length 100 mm, Shanghai Great Wall Scientific Instrument Store, China) to gel for 24 h at 37 °C. Four different kinds of Pdots were added into capillary tubes for free diffusion. Then, the capillary tubes were observed via inverted fluorescence microscope (IFM).

2.6. Ex vivo inverted fluorescence microscope (IFM) imaging of lymphatics

All animal procedures were performed in accordance with the Guidelines for Care and Use of Laboratory Animals of Shanghai Jiao Tong University, and experiments were approved by the Animal Ethics Committee of Shanghai Jiao Tong University (Shanghai, China). All the ICR white mice and Balb/c nude mice were anesthetized with 1% sodium pentobarbital solution. After immobilizing the mouse limbs, cut along the midline of the abdomen in the mouse. Unfold the skin adhered to the peritoneum, and inguinal lymph node (LN) can be seen on both sides of the mouse. The syringe pump (Legato 788130, KD Scientific Inc., USA) was utilized with the insulin syringe to inject Pdots into inguinal LN. The parameter settings are listed as molecular weight (average M_w = 19000, average $M_n \leq 25000$ and average M_w = 47000), ligand (PS-PEG-COOH and MMA-NH_2), injection volume (1 μL and 8 μL) and imaging time point (5 min and 24 h) in Table S3. Then, the specimen including inguinal LN, axillary LN and LV were cut from the mouse which were attached to the peritoneum. Put the tissue on the object slide and spread it. Finally, image the specimen with shunyu xd30 fluorescence microscope (Beijing jiayuanxingye Biotech Co.Ltd, China).

Furthermore, two probes as Pdots and carbon nanoparticles (NPs) suspension (Chongqing Lummy Pharmaceutical Co., Ltd., China) were used together for visual and fluorescent dual channel imaging. Carbon NPs suspension was injected 30 min earlier than Pdots, and after 30 min of injecting Pdots and carbon NPs, the collecting LV was imaged.

2.7. Establishment of animal model

Human ovarian adenocarcinoma cell line SKOV3 was purchased from Cell Bank of Chinese Academy of Science (Shanghai, China). SKOV3 cells were grown in McCoy's 5A medium. The following incubation procedures were the same as normal. To establish the model of subcutaneous tumor-bearing mice, 150 μL of SKOV3 cells (5×10^6 cells mL−1) was injected subcutaneously into the ass of nude mice. Tumor volume reached above 250–350 mm^3 after 21–28 d of inoculation in SKOV3 tumor models.

2.8. In vivo stereomicroscope and stereoscopic fluorescence microscope (SFM) imaging of lymphatics

The anatomical procedure was similar. After flatting and fastening the skin, image the interested region from inguinal LN to axillary LN on both sides of the mouse. The difference between stereomicroscope and stereoscopic fluorescence imaging was the fluorescence channel. Olympus sz61 stereoscopic microscope (Beijing jiayuanxingye Biotech Co., Ltd., China) was used to observe the anatomical steps in the bright field. YHZ16 stereographic fluorescence microscope (Shanghai Yuehe Biotech Co., Ltd., China) had four channels. Bright field and B channel (E_x = 470 nm/40 nm, E_m = 544 nm/50 nm) were used in the experiment. To obtain

the single clear collecting LV, two microscope forceps worked together and removed the enveloping mucous membrane around inguinal LN, collecting LV and axillary LN. Besides, the clean tissue which was put on the object slide was imaged in the B channel. Furthermore, after injecting Pdots for a period of time, the same inguinal LN was injected with PBS for observing the changes of lymphatics. Also, the observation of Pdots in LVs and LNs were conducted by injecting Pdots firstly and anatomized after 1 d, 3 d, 5 d, 7 d, 14 d, 21 d and 28 d of injection.

2.9. *In vivo probe-based confocal laser endomicroscope (pCLE) imaging of lymphatics*

The Cellvizio® Dual Band system pCLE (Mauna Kea Technologies, France) was conducted *in vivo* for further high-resolution imaging. In this experiment, the parameter setting, imaging method and analysis process were the same as that in former published articles [18,19,21].

2.10. *The immersion staining of LN and LV*

Four different proportions of Pdots (**2.5 PC**, **2.5 PN**, **4.7 PC** and **4.7 PN**) were applied in the experiment. The immersion ways were split into the removed fresh or fixed LNs directly putting into 100 μL solutions. Gradient solutions were divided into five groups: ten times concentrated, five times concentrated, two times concentrated, original and diluted half solutions. After 48 h, 72h or 96 h, the LNs connected with LVs were imaged by confocal laser scanning microscope (CLSM) (Leica, Germany). Two different channels were set: **4.7PC/4.7 PN** (excitation 405 nm, emission 500–600 nm), **2.5PC/2.5 PN** (excitation 458 nm, emission 500–600 nm).

2.11. *Immune cells of LN uptake experiments*

The experimental and control groups were injected by Pdots and normal saline solution, respectively. The parameter settings were as followed: injectant (**2.5 PC**, normal saline solution), speed (3 s, 1 min), volume (15 μL) and imaging time point (5 min, 24 h, 72 h). After the mouse was sacrificed, axillary LNs on injection sides were removed and placed in a petri dish. The dish was observed under the stereomicroscope, and all attached adipose tissue was pruned away. Then, axillary LNs were rinsed with PBS. After 3 h incubation with 1.5 mg/mL collagenase IV (40507ES60, Yeasen, China) at 37 °C, axillary LN were gently separated through a 70 μm cell strainer using a 15 mL syringe plunger, and the strainer was thoroughly washed by FACS buffer of 1% bovine serum albumin (BSA, MB4219, meilunbio, China) in 1 × PBS. The cell suspension was transferred into the tube (352063, Corning Falcon, USA) on ice, and centrifuged at 1000 r/min for 5 min at 4 °C. Pour off the supernatant. Cells were incubated with 100 μL Zombie NIR™ fixable dye (423105, APC-Cy7, Biolegend, USA) for 20 min on ice in dark. After washing and centrifugation, cells were then separated into two groups and incubated with a cocktail of antibodies for 20 min on ice in dark: Biolegend Percp-Cy5.5 CD3, Biolegend PE-Cy7 CD4, Biolegend PE CD8; Biolegend BV421 B220, Biolegend APC CD169, Thermo Fisher Scientific PE-Cy7 CD11b, Thermo Fisher Scientific PE CD11c, Thermo Fisher Scientific Percp-Cy5.5 F4/80 (Thermo Fisher, USA). Finally, the washed cells were resuspended in PBS for further analysis. Data was acquired using a FACSAria II flow cytometry (Becton Dickinson, USA), and analyzed via FlowJo software. Cell types were defined as follows: T cells: $CD3^+$, $CD4^+$ T cells: $CD4^+CD3^+$, $CD8^+$ T cells: $CD8^+CD3^+$, B cells: B220+, Monocytes: B220-CD11c-CD11b + F4/80 + CD169-, subcapsular sinus macrophages (SSMs): B220-CD11c+CD11b + CD169 + F4/80-, medullary sinus macrophages (MSMs): B220-CD11c+CD11b + CD169 + F4/80+, medullary cord macrophages (MCMs): B220-CD11c+CD11b + CD169-F4/80+, plasmacytoid dendritic cells (pDCs): CD11c+CD11b-B220+, conventional dendritic cells (cDCs): CD11c+CD11b-B220- [25]. The excited and emission wavelength of the material were closer to FITC channel. Also, normal saline solution groups were performed as the same procedure and data processing.

2.12. *Ex vivo two-photon microscope (TPM) imaging of lymphatics using uDISCO*

All the tissues of nude mice were conducted in the same way for transparency [19,21]. Briefly, immerse the fixed specimen in PBS for washing. Then, keep it in the gradient of dehydration as 30% *tert*-butanol for 4 h, following 50%, 70% for overnight, 80%, 90%, 96% for overnight. Eventually, incubate it in BABB-D4 solutions for optically transparence [24]. Fluorescence images were acquired using a Leica TCS SP8 STED 3X microscope equipped with the HCX PL APO CS 10 × /0.40 DRY objective, HC PL APO CS2 20 × /0.75 DRY objective, HC PL APO CS2 40 × /1.10 WATER objective or HC PL APO CS2 63 × /1.40 OIL objective (Leica, Germany). The yellow channel (Ex = 740 nm, Em = 500–600 nm) was imaged for fluorescent Pdots.

2.13. *Histology*

The specimen of axillary LN was removed from the mouse and immediately embedded in the optimum cutting temperature compound (SAKURA, USA) at −80 °C. The frozen tissue was cut into 8 μm sections, fixed with 4% paraformaldehyde and stained using hematoxylin (MB9898, meilunbio, China). Then, the hematoxylin and Pdots were observed via the bright field channel, fluorescence channel and overlay channel of IFM.

2.14. *Staining of the whole axillary LN and collecting LV*

The removed axillary LN connected with collecting LV injected via 15 μL Pdots within 3 s for 5 min were fixed with 4% paraformaldehyde. Besides, the fixed sample was placed in 1 mL of the blocking solution (2% W/Vol BSA in PBS, 0.3% vol/vol Triton X-100) at room temperature for 24 h. Then, put the sample into 4′,6-diamidino-2-phenylindole (DAPI) solution (MA0128, meilunbio, China) for nuclear staining and DiD solution (5 μM, MB6190, meilunbio, China) for cytomembrane staining. Each staining period last for 5 h, and washing solution containing 0.2% vol/vol Triton X-100 was used after each staining period for 24 h [26]. Using a Leica TCS SP5 CLSM, three different channels were as follows: fluorescent Pdots (excitation 458 nm, emission 530–600 nm), DAPI (excitation 405 nm, emission 425–500 nm), and DiD (excitation 633 nm, emission 655–675 nm).

2.15. *Immunostaining of the whole transparent axillary LN*

The first two steps including fixation and blocking process were the same as above. Then, followed by 3 d of primary antibody (PROX1, 1:800 dilution, ab101851, Abcam, UK) staining in fresh blocking solution at 37 °C with shaking. Next, samples were washed and shaken twice with 0.2% vol/vol Triton X-100 for 12 h each time at room temperature. The secondary antibody (Donkey Anti-rabbit, 1:500 dilution, abs20009, Absin, China) staining was performed under the same conditions as for the primary antibody. Besides, the DAPI staining and uDISCO process were the same [26]. The PROX1 channel setting of TPM imaging was the excitation of 633 nm and the emission from 650 to 670 nm.

2.16. *Immunofluorescence of the axillary LN and collecting LV frozen section*

The fresh tissue injected with 15 μL Pdots within 3 s for 5 min was immediately frozen below −80 °C and cut into 8 μm sections. The section was fixed with 100% precooled methanol for 10 min and washed in PBS for 5 min three times. For permeation, 0.3% Triton X-100 was used at room temperature for 10 min. The washing process was in PBS for 5 min three times. Then, blocking solution (derived from 10% of the serum of the species producing the secondary antibody, 1% BSA, 0.3 mol/L

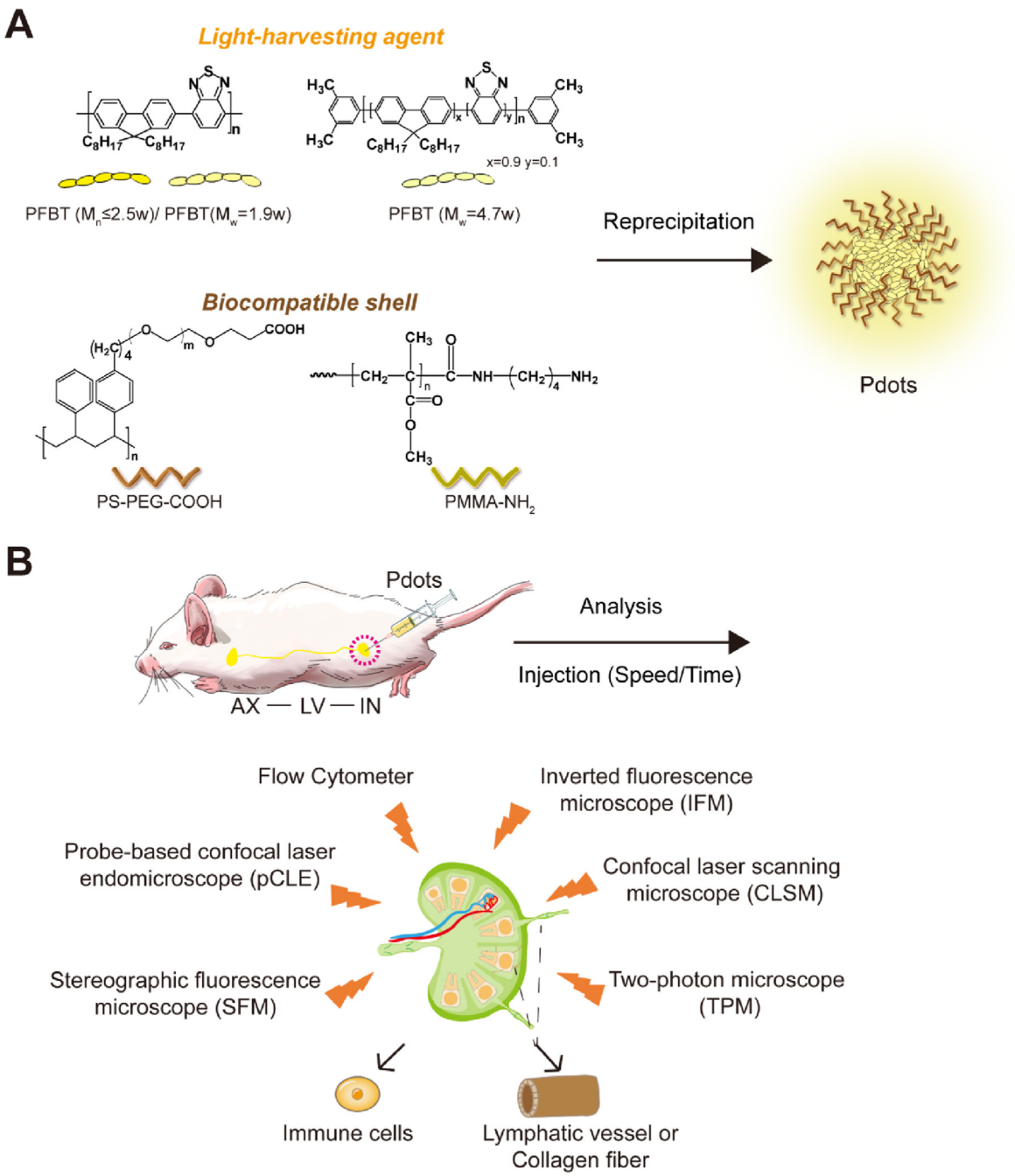

Scheme 1. A) Chemical structures of PFBT (M_n < 25000), PFBT (M_n = 19000), PFBT (M_n = 47000), PS-PEG-COOH, and PMMA-NH_2, and the reprecipitation of polymer dots (Pdots). Pdots are prepared via one of light-harvesting agents and one of biocompatible shells. B) The schematic depicted the selection, and lymphatic imaging of Pdots. The relationship between Pdots and immune cells or channels in the LNs and LVs was studied by using multiple imaging microscopy, including inverted fluorescence microscope (IFM), probe-based confocal laser endomicroscope (pCLE), stereographic fluorescence microscope (SFM), confocal laser scanning microscope (CLSM), two-photon microscope (TPM), and flow cytometer.

glycine solution, prepared with PBS) was dropped on the section at room temperature for 1 h without washing. Subsequently, add the primary antibody (podoplanin, 1:800 dilution, 14-5381-82, Thermo Fisher, USA; CD31, 1:50 dilution, ab7388, Abcam, UK) diluted by universal antibody diluent (WB100D, New Cell& Molecular Biotech Co., Ltd, China) for incubation in a humidified box at 4 °C overnight (≥16 h). Afterwards, the sample section was taken from the refrigerator and placed at room temperature for at least 30 min. The washing process was in PBS for 10 min three times. Subsequently, the secondary antibody (Goat anti-Hamster, 1:400 dilution, A-21112, Thermo Fisher, USA; Goat anti-rat, 1:500 dilution, 4418S, Univ, China) diluted by universal antibody diluent was added on the section at 37 °C for 1 h, and washed off via PBS for 15 min three times. Finally, the tissue section was covered using antifade mounting medium with DAPI for at least 20 min and sealed via nail polish for four corners of the coverslip. Using a Leica TCS SP5 CLSM, three different channels were as follows: fluorescent Pdots (excitation 458 nm, emission 530–600 nm), DAPI (excitation 405 nm, emission 425–500 nm), podoplanin (excitation 561 nm, emission 595–615 nm), and CD31 (excitation 633 nm, emission 645–665 nm).

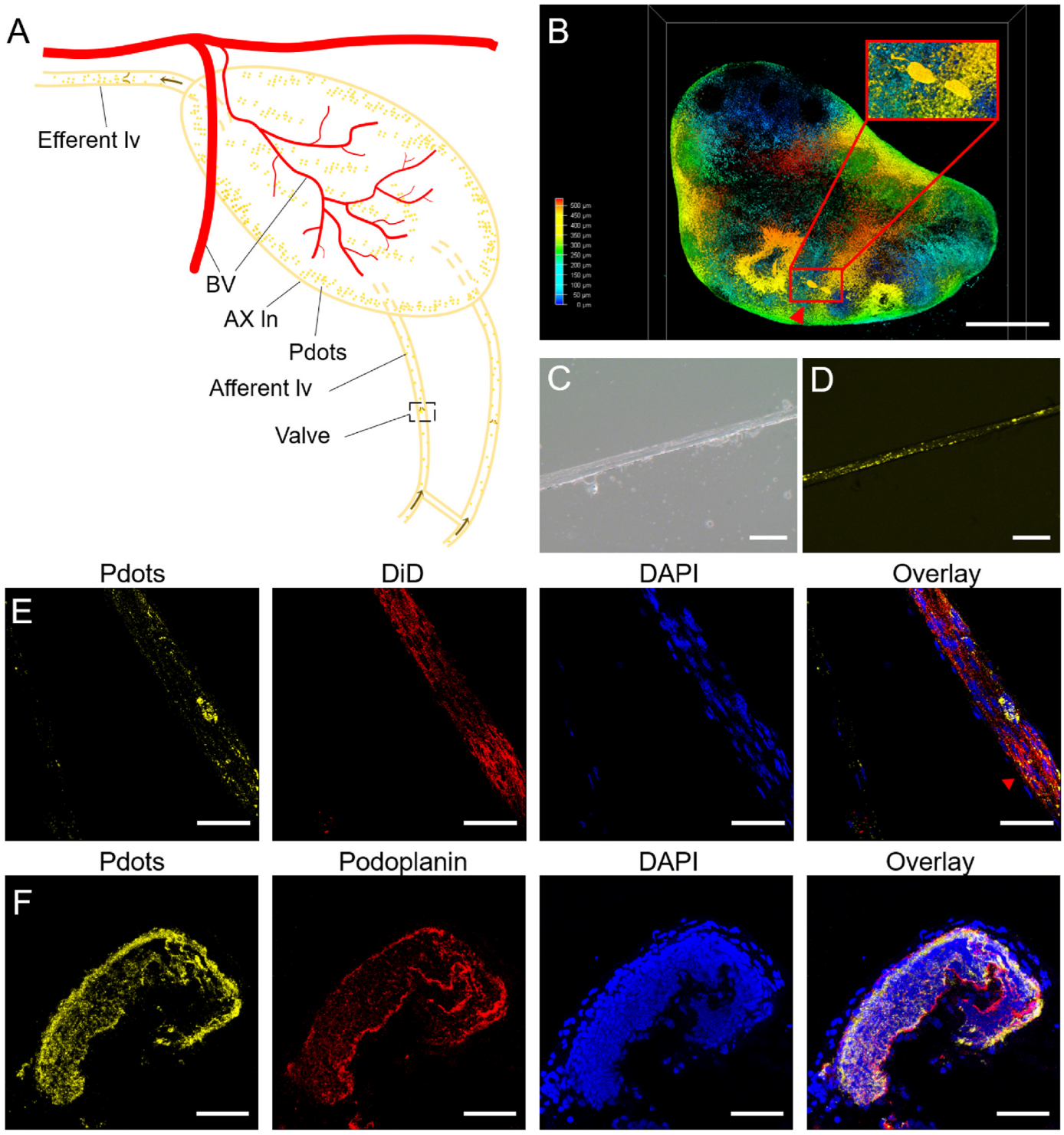

Fig. 1. The imaging of lymphatic system injected via Pdots. A) The simple drawing of axillary lymph node (LN) connected with afferent and efferent lymphatic vessels (LVs) imaged by Pdots. B) The TPM image of axillary LN and connected afferent LV which red triangle points at. The red box represents the magnified connected afferent LV. C-D) The brightfield and fluorescence channel of stripped collecting LV were taken by SFM *ex vivo*. E) The CLSM imaging of the whole collecting LV includes Pdots channel, DiD cytomembrane channel, DAPI cytoblast channel, overlap channel. F) The CLSM imaging of the collecting LV frozen section includes Pdots channel, Podoplanin LV channel, DAPI cytoblast channel, and overlap channel. Red triangles point at the connected LV in B and the Pdots aggregation sites in E. Scale bars represent 500 μm in B, 100 μm in C-D, and 50 μm in E-F, respectively. (For interpretation of the references to color in this figure legend, the reader is referred to the Web version of this article.)

2.17. Silver staining of collagen fiber in the axillary LN

The 10 μm frozen section of injected axillary LN was fixed with 4% paraformaldehyde for 10 min and washed for 2 min. Then, the silver staining was performed using ProteoSilver™ kit (PROTSIL1, Merck, USA). The sensitizer solution, silver solution and developer solution were prepared according to the corresponding steps. In brief, the section was dipped in the silver and developer solution for 10 min, and washed with

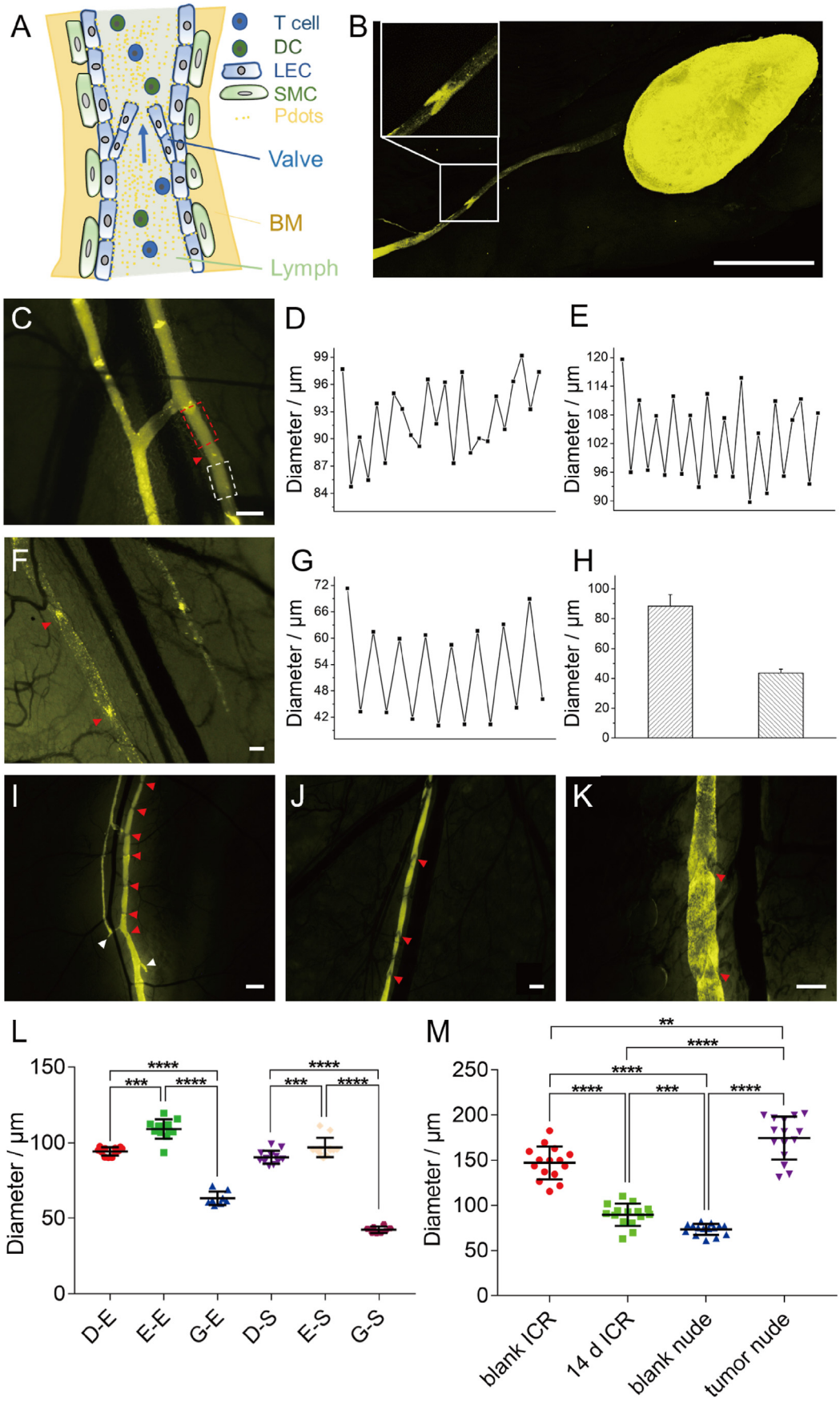

(caption on next page)

Fig. 2. The observation of lymphatic valves and changes in LVs. A) The schematic diagram of collecting LV including lymphatic valve imaged by Pdots. B) The 3D picture of lymphatic valve, collecting LV and LN imaged by Pdots. The white box represents magnified lymphatic valve. C) The screenshot of the contraction and relaxation in collecting LV imaged via SFM after injection of Pdots. D-E) The different diameters change line charts of the collecting LV labelled by the red and white dashed box in B. F) The SFM image of LV at 14 d post-injection of Pdots. G) The different diameters change line charts of the collecting LV 7 d post-injection of Pdots in Figure S5C. H) The diameter of the LV 28 d post-injection of Pdots in Figure S5E and F. I) The branches and lymphatic valves of lv 5 min post-injection. J-K) The lymphatic valves of lv 5 min post-injection in nude mouse and tumor mouse, respectively. L) The comparison between diameters of expansion and shrinkage in lymphatic vessels is shown as mean ± SD from 5 min in D and E and 7 d in G after injection of Pdots. D-E, E-E and G-E represent the diameter measurement of every expansion in D, E and G, respectively. D-S, E-S and G-S represent the diameter measurement of every shrinkage in D, E and G, respectively. M) The diameter comparison of LV among 4 min-imaging of blank 3-week-year-old ICR mouse in I, 14 d-imaging of ICR mouse in F, blank nude mouse in J and tumor mouse in K is shown as mean ± SD. Red triangles point at lymphatic valves, and white triangles point at the branches of LV. $^{***}P < 0.001$. Scale bars represent 2 mm in B, 100 μm in C and F, 500 μm in I, and 200 μm in J and K, respectively. (For interpretation of the references to color in this figure legend, the reader is referred to the Web version of this article.)

water for 10 min and 1.5 min after the two former solutions. After the 10 min function of developer solution, add 20:1 vol/vol stop solution for 5 min co-incubation, and immerse in the water for 15 min. Eventually, the sample section was dehydrated with gradient ethanol and transparentized via dimethylbenzene based on conventional procedures.

3. Results

3.1. Synthesis and characterization of Pdots

To compare the effects of molecular weights and surface modification on the lymphatic imaging, we designed and synthesized five PFBT Pdots (Scheme 1A). The size, Zeta potential, UV–vis absorbance and fluorescence emission spectra of Pdots were shown in Figure S1. The size of Pdots with PS-PEG-COOH was around 40 nm, which was smaller than that of Pdots with PMMA-NH_2 (100–120 nm) as shown in Figure S1A. The Zeta potential of five Pdots was from −25 mV to −30 mV as shown in Figure S1B. The normalized UV–vis absorbance of Pdots (PFBT average $M_w = 19000$ and average $M_n \leq 25000$) showed a maximum at 468 nm of **1.9 PC**, 471 nm of **2.5 PC**, and 469 nm of **2.5 PN** as shown in Figure S1C. Comparatively, **4.7 PC** or **4.7 PN** had the apex at 380 nm or 383 nm. The peaks were in descending order as **4.7 PC**, **2.5 PC**, **2.5 PN**, **1.9 PC** and **4.7 PN**. Figure S1D exhibited an emission peak around 543 nm and the descending order was **4.7 PC**, **1.9 PC**, **4.7 PN**, **2.5 PC** and **2.5 PN**. All these results indicated synthesized Pdots had applicable particle sizes and good colloidal stability in water, and the fluorescence intensity was high enough for imaging lymphatics. The relationship between Pdots and immune cells or channels in the LNs and LVs was studied by using multiple imaging microscopy, including inverted fluorescence microscope (IFM), probe-based confocal laser endomicroscope (pCLE), stereographic fluorescence microscope (SFM), confocal laser scanning microscope (CLSM), two-photon microscope (TPM), and flow cytometry, as displayed in Scheme 1B. The advantages, disadvantages and complementarities of five imaging methods are also compared in Table S2. To obtain comprehensive analysis, different ways were used for exploration and verification.

3.2. The comparison of lymphatic imaging with different Pdots and injection parameters

A simple drawing of axillary LN which is in the access from the inguinal LN is displayed in Fig. 1A. The injection parameters of Pdots were screened to find the optimal imaging results of LVs and LN. Imaging results (Table S3) showed that 1 μL of injection volume only displayed the collecting LV, while 8 μL of injection volume displayed the collecting LV and axillary LN simutaneously. The adherence of Pdots loaded with PMMA-NH_2 on the collecting LV was more than Pdots loaded with PS-PEG-COOH, while Pdots with PS-PEG-COOH were more well-distributed in the lymphatics compared to Pdots with PMMA-NH_2. In addition, due to the change of signal intensity in different time points, Pdots with PMMA-NH_2 are appropriate for imaging collecting LVs at short time points, and Pdots with PS-PEG-COOH are suitable to image collecting LNs at long time points. In order to obtain simultaneous imaging of LN and LV, Pdots with carboxy group were applied in following experiments.

3.3. The distribution of Pdots in the LVs

As shown in Fig. 1B, Pdots aggregated in the junction of connected LV and axillary LN like a 'flower'. After treatment of organic reagent in the transparence process, the signal intensity of Pdots had no significant difference from the original picture (Figure S2A-B), which indicated good photostability of Pdots. In Figure S2C-F, one or two LVs connected with axillary LN can be imaged via IVM. The fluorescence channel and brightfield channel of single LV in Fig. 1C and D was observed with dot signals on the semitransparent wall. The confocal image of single LV in Fig. 1E displayed Pdots existed in the extracellular space. In addition, the partial overlap between Pdots channel and LV channel in the frozen section of Fig. 1F showed Pdots were stronger in the outer layer of LV. These results verified that Pdots were mainly distributed in the extracellular space of collecting LVs endothelial cells.

The immersion experiment was conducted to test whether Pdots could migrate into axillary LN and LV without the transportation of lymph. Figure S3A showed only fresh LV immersed in **4.7 PN** could be imaged as dot and clump signals. After LNs were fixed, the incubated Pdots were unlikely to get into the tissue in Figure S3B. The signal of injection method was uniform and the imaging speed was fast. However, the signal of soak method was chaotic. With the immersion time getting longer, the LN became softer and the structure changed. Additionally, the diluted Pdots solution was unable to image lymphatics, and the ten times concentrated Pdots solution was easy to agglomerate (Figure S3C). The results suggest that the immersion solution containing Pdots with PMMA-NH_2 have the ability of migrating to image the LV wall actively.

3.4. The signal aggregation and diameter change around the lymphatic valve in the LV

The schematic diagram exhibits the structure of lymphatic valve in Fig. 2A. The lymphatic valve was captured via SFM, pCLE and TPM as shown in Figure S4A-B and 2B, respectively. During the observation process of the lymphatic valve immediately after injection, the imaging of contraction and relaxation of LV was record (Fig. 2C, Video S1). In comparison between the upstream and downstream of the lymphatic valve, the diameter change trend was similar, but the upstream changed more, and the largest gap was up to 23.6 μm that was nearly two times than 12.9 μm of downstream (Fig. 2D and E). It is potential that the upstream needs higher pressure to promote the lymph with Pdots to cross the lymphatic valve in limited time. The average of every shrinkage interval time is 17.63 ± 3.34 s analyzed in Table S4.

Supplementary data related to this article can be found at https://doi.org/10.1016/j.mtbio.2022.100317.

Due to the strong signal of valve, it intrigued us to observe the change process after injection of Pdots and PBS. At first, the existence of signal still imaged the LV at 30 min post-injection and changed a little after 15 min in Figure S4C. After the washing of PBS, the signal intensity got lower, and the structure of lymphatic valve became clear in Figure S4D.

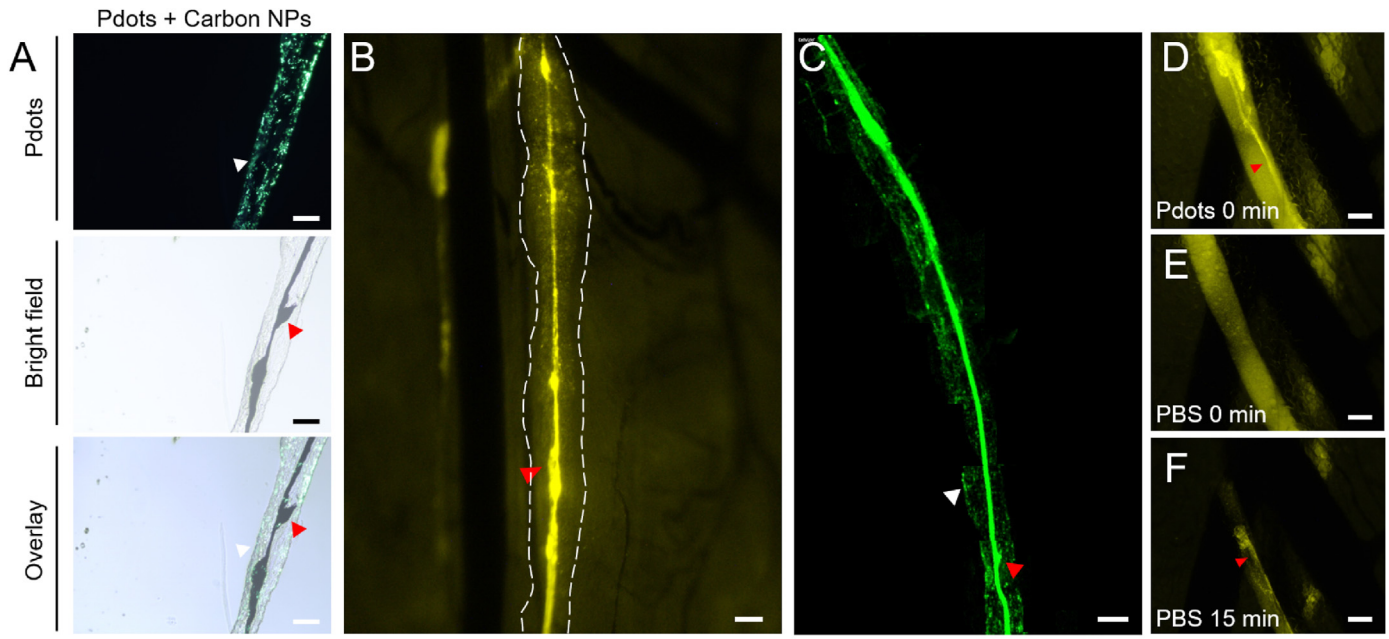

Fig. 3. The observation of PV inside the LV. A) Two channels including Pdots channel and Carbon NPs channel drew the outline of LV and PV imaged by IFM. B–C) The SFM and pCLE images of PV in the collecting LV. D-F) The changes of PV in the collecting LV were imaged immediately after injection of Pdots, and 0 min and 15 min after injection of PBS via SFM. Red triangles point at PV inside the LV, and white triangles point at the outer LV. Scale bars represent 100 μm. (For interpretation of the references to color in this figure legend, the reader is referred to the Web version of this article.)

Then, in Figure S4E and F at 1 h post-injection, the strip-arranged LV was followed by the intercellular-distribution LV, and the structure was around the lymphatic valve. In addition, Pdots in the LV distributed in mainly two kinds of signal shapes as strip and intercellular-distribution.

Furthermore, the description of LV was observed clearly within a period of time. As shown in Figure S5A and B after injecting Pdots of 5 d, there was an additional LV besides the main collecting LV displaying obvious Pdots aggregations with regular intervals, and the intersection in the LV and the blood vessel leaked a few Pdots into surroundings. Prolong the time to 7 d in Figure S5C, only the LV close to the blood vessel had a faint outline. The imaging of contraction and relaxation in the LV was recorded in Video S2 and analyzed in Fig. 2G. The regular changes ranged from 40.09 μm to 71.33 μm, and the average of every shrinkage interval time was 26.57 ± 12.54 s analyzed in Table S5. The diameter was largely smaller than that at 5 min post-injection because the Pdots solution filled in the LV at the beginning. To drain the added solution and return to normal, the shrinkage frequency at 5 min post-injection was higher. The lymphatic valve in the collecting LV was imaged after 7 d *ex vivo* or 14 d *in vivo* injection of Pdots as shown in Figure S6 and Fig. 2F, respectively. The imaging time of LV last up to 21 d as shown in Figure S5D. Intriguingly, the partial leaked Pdots helped image the contraction and relaxation of LV even after 28 d as shown in Figure S5E and F. The diameter in Fig. 2H changed from 88.47 μm to 43.63 μm as similar to that of 7 d imaging. The diameter change difference of expansion or shrinkage in Fig. 2C and F was compared and analyzed in Fig. 2L. There are significant differences of diameter in LVs at every expansion or shrinkage between different imaging time points. As shown in Figure S7, the axillary LN was still bright for observation at 28 d post injection. Pdots signals mostly distributed in the outer layer with the normal cell morphology. Basically, with the time going, Pdots in the LV went into the next LN, branch LV or the surroundings from the main LV. It is possible that the driving force of lymph made Pdots move.

Supplementary data related to this article can be found at https://doi.org/10.1016/j.mtbio.2022.100317.

Furthermore, the imaging results of single collecting LV in 3-week-year-old ICR mouse, blank Balb/c nude mouse and tumor Balb/c nude mouse were compared in Fig. 2I–K. The interval of lymphatic valve in Fig. 2F 14 d post-injection was 712.75 μm, and the diameter of LV was 89.72 ± 12.34 μm. The interval of lymphatic valve in Fig. 2I of 3-week-year-old mouse 5 min post-injection ranged from 532.51 μm to 789.19 μm with the mean of 683.32 ± 94.06 μm, and the diameter of LV was 147.04 ± 18.25 μm. In addition, the sprout pointed at via white arrows grew from the main LV. The diameter difference mean the injected Pdots put higher pressure on the LV wall and lead to the expansion. In nude mouse of Fig. 2J, the mean interval was 809.25 ± 356.78 μm, and the diameter of LV was 73.50 ± 18.25 μm. In tumor mouse of Fig. 2K, the interval was 642.03 μm, and the diameter of LV was 174.68 ± 23.83 μm which was greatly larger than that of normal LV. Therefore, the distance between two lymphatic valves is from 532.51 μm to 1061.03 μm, and there is no distinct interval difference in different animal models. Meanwhile, the diameter difference of LV was compared in Fig. 2M. There are significant differences except for the difference between 5 min imaging of blank ICR mouse and tumor nude mouse. These results showed that Pdots can image the LV and lymphatic valve steadily and continuously, and help observe the contraction and relaxation of LV.

3.5. *The floating change process of primo vessel (PV) in the LV imaged via Pdots*

Up to now, the related real-time imaging articles on PV are still limited [27]. A section of vessel floating freely in the LV was frequently imaged in SFM and pCLE videos. It is obvious that the PV imaged by carbon NPs in the bright field had the uneven diameter with the irregular spine as shown in Fig. 3A. The PV was recorded in the middle of LV and brighter than the around wall as shown in Fig. 3B and C. In addition, Pdots could image the PV brightly at 24 h post-injection as shown in Figure S8A. In Fig. 3D-**E**, the fluorescence intensity of LV got lower, and the PV was washed away when injected with PBS immediately. At 15 min post-injection, the LV turned into the original diameter and the partial was bright (Fig. 3F). During the anatomy process, the bottom PV was pushed to the top via microscopic forceps and piled up as shown in Figure S8B. The frozen section of LV including PV in Figure S8C displayed most of Pdots assemble in the inner PV instead of the outer LV wall. It is possible that PV plays the role of absorbing foreign bodies in the

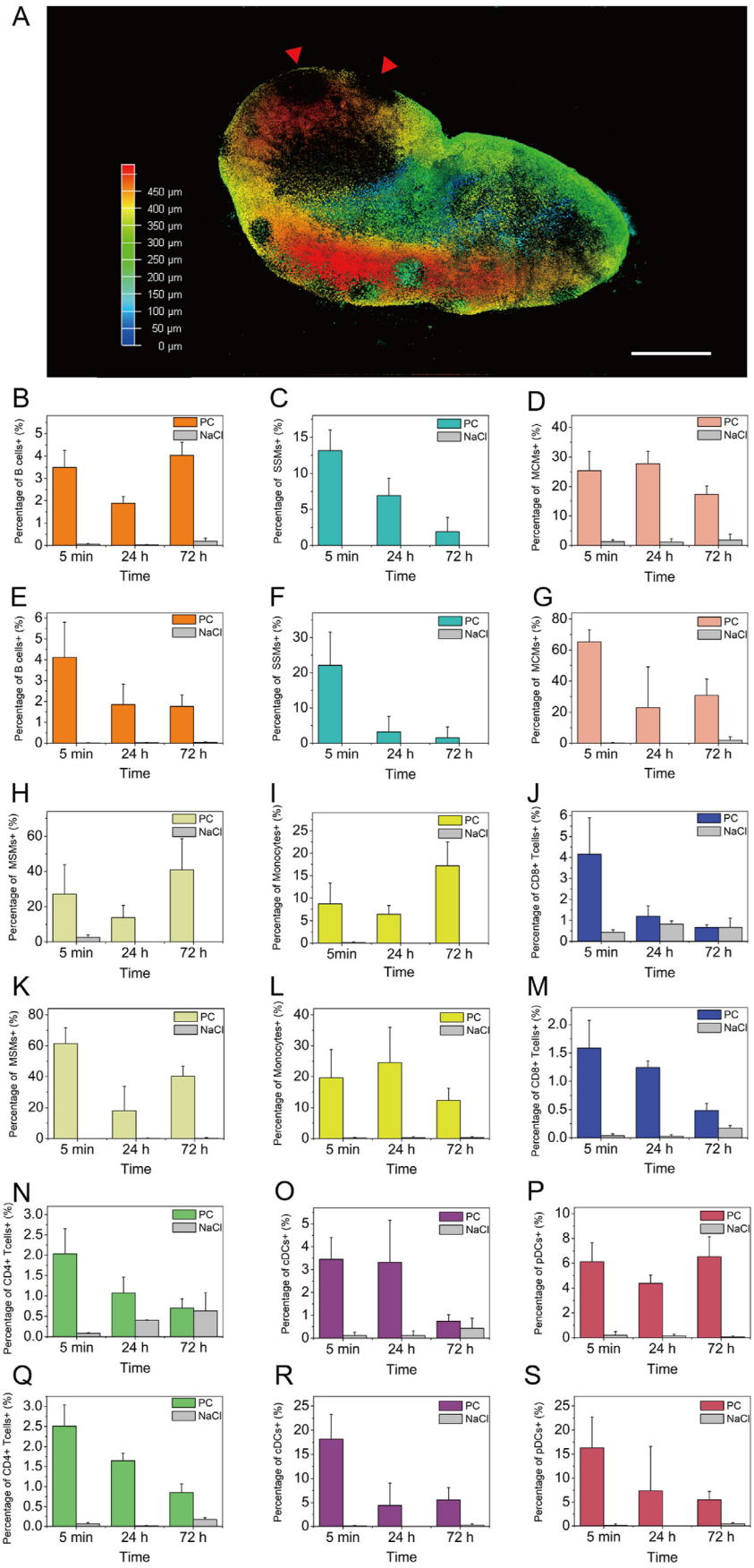

Fig. 4. The relationship verification between Pdots and immune cells in LN via imaging and flow cytometry database. A) The 3D TPM image of axillary LN with the injection of 15 μL Pdots in 1 min after 24 h. B–I, K-L) The relevance between Pdots and four kinds of cells as B cells, SSMs, MCMs, MSMs and monocytes at different time points of 5 min, 24 h and 72 h. The experimental and control groups are based on two rates of 3 s and 1 min injected via Pdots and normal saline solution, respectively. J, M – S) The relevance between Pdots and $CD4^{+}$/$CD8^{+}$ T cells or pDCs and cDCs. Red triangles point at B cell zone. The injection time is 1 min in B-D, H-J and N–P, and the injection time is 3 s in E-G, K-M and Q-S. Scale bar represents 500 μm in A. (For interpretation of the references to color in this figure legend, the reader is referred to the Web version of this article.)

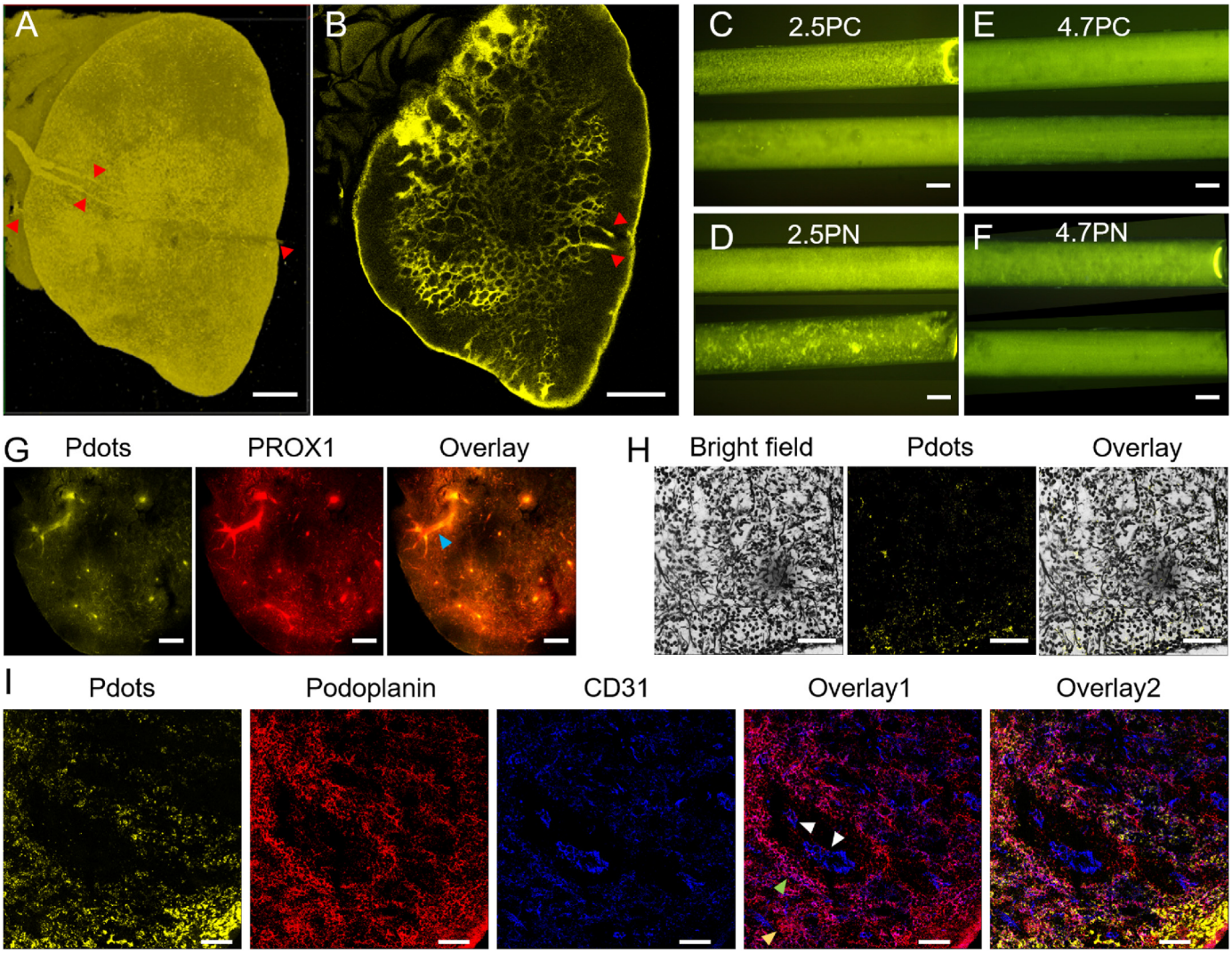

Fig. 5. The relationship verification between Pdots and channels in LN. A-B) The TPM 3D image and single picture of axillary LN includes four vessels pointed by red triangles. C–F) The penetration of Pdots in collagen hydrogels including 2.5 PC, 2.5 PN, 4.7 PC and 4.7 PN was imaged by IFM in vitro. The top row represents empty capillary tubes, and the bottom row represents capillary tubes filled with collagen hydrogels. G) The transparent axillary LN includes Pdots channel, PROX1 channel and overlay channel was imaged via FCFM. H) The relationship between Pdots and collagen fibers was imaged via silver staining. I) The axillary LN frozen sections include Pdots channel, podoplanin channel, CD31 channel and two overlay channels were imaged via FCFM. Overlay1 includes podoplanin channel and CD31 channel. Overlay2 includes Pdots channel, podoplanin channel and CD31 channel. Red triangles point at the connected LV of axillary LN in A and B. Blue triangles point at the large LV containing yellow Pdots signals in G. White triangles point at blue blood endothelial cells, green triangles point at purple lymphatic endothelial cells, and yellow triangles point at red fibroblast reticular cells in I. Scale bars represent 500 μm in A-B, 100 μm in C–F, 200 μm in G, and 50 μm in H and I, respectively. (For interpretation of the references to color in this figure legend, the reader is referred to the Web version of this article.)

LV, and it leaves from the LV to the LN with the absorbates.

3.6. The relationship between Pdots and immune cells in the LN

In order to distinguish the distribution region inside the LN, different parameter settings of imaging time point and injection speed were applied for comparison. As shown in Fig. 4A of 3D TPM image, it is obvious that no bright signal existed in B cells zone at 24 h post-injection, and this is consistent with the percentage of B cells+ which were all below 4% in flow cytometry data of Fig. 4B and E. These results indicated Pdots had no relationship with B cells.

For different zones of macrophages in Fig. 4C–D and H and **4F-G and K**, the entire group of 5 μL/s injection speed had more cells associated with Pdots at 5 min post-injection. When firstly injecting Pdots into axillary LN, the outmost defense SSMs phagocytosed large amounts of strange invaders. The percentage got the peak at 13.15% or 22.08% and went down to 1.92% or 1.54% with the time going. As the macrophages upgraded, the previously existed Pdots were processed or transferred. The faster injection speed led more SSMs to associate with Pdots in Fig. 4C and F. With regard to MCMs, the relevant percentage became up as from 25.4% to 27.73% and down to 17.38% for the injection of 15 μL/min, but another group went from 65.35% to 22.97% and to 30.8% in the reverse trend. The faster injection speed lead nearly two times more MCMs to relate to Pdots at 5 min in Fig. 4D and G. The middle time point was opposite to the developing trend, and we speculate that the disordered period was the former step to be stable. The process meant the first chaotic state at 5 min post-injection when Pdots just flowed into axillary LN, the next intermediate state at 24 h post-injection when Pdots switched to moving or stopping, and the final stable state at 72 h post-injection when Pdots already existed in some places. The last focus MSMs was shown as 27.18%, 13.73% and 40.93% or 61.4%, 18.04% and 40.33% in Fig. 4H and K. Two groups had the similar histogram trend with that of Fig. 4G. The percentages of MSMs+ in two groups were almost equal at 72 h. The comparison in the same group with different

kinds of macrophages displayed the moving routine started from subcapsular sinus, passed medullary cord, and got to medullary sinus. In general, the relevance between macrophages and Pdots is due to cell location, injection speed and imaging time point.

Monocytes also have phagocytosis and clearance functions. In Fig. 4I and L, two groups of injection speed 15 μL/min (8.75%, 6.43% and 17.23%) and 5 μL/s (19.65%, 24.53% and 12.32%) had totally different change trends. The percentage was higher at the beginning and got lower in the end of the faster injection speed group. This showed Pdots made effect on partial monocytes. Additionally, the high-resolution picture in Figure S9 guided the distribution of different signals as related to immune cells or channels. Round signals are likely to exist in cells of the outer layer versus stripped signals are likely to distribute in channels of the inner layer. Further on, in Figure S10, the location relationship between Pdots and DiD display Pdots existed in the extracellular space along the strip structure or around the nucleus.

The relationship between other immune cells as DCs or T cells and Pdots was further studied. As the trends went down with the time getting longer in Fig. 4J and N and M and Q, the percentages of connected cells were very low. It indicated that Pdots affected T cells a little without causing strong and specific immune response. Comparatively in Fig. 4R and S, the percentages of cDCs+ and pDCs+ decreased gradually from 18.18% or 16.3%–5.57% or 5.53% in the faster injection speed group, respectively. Moreover, the percentage of cDCs+ and pDCs+ retained below 4% and nearly 6% all the time in the slower injection speed group of Fig. 4O and P. This showed the high pressure affected the relationship between Pdots and DCs well after the initial injection, and last not very long. With the time going, Pdots in cells were digested or carried away. to These results indicated that Pdots are relevant to phagocytic cells such as macrophages and monocytes in spite of the change of injection speed or imaging time point.

3.7. The transportation of Pdots in the LVs or collagen fibers of LN

In consideration of the possibility of Pdots transportation via channels, the verification about collagen fibers and LVs was carried out in the axillary LN. Combining 3D picture (Fig. 5A) and section picture (Figure S11A), three LVs were linked to the LN. The whole bright structure interweaved, and vessels connected with each other as shown in Fig. 5B. Additionally, the structure seemed to start from two vessels as shown in Fig. 5B and S11B. It is likely to light up the LN via the bond of partial immune cells and vessels. Figure S11C and D showed Pdots distributed along the blood vessel. Then, to simulate collagen situation of four different Pdots in the LN, collagen hydrogels were built in the capillaries (Fig. 5C–F). When the size distribution was similar, three kinds of Pdots including **2.5 PC**, **4.7 PC** and **4.7 PN** changed a little in blank capillaries and collagen hydrogels, even it looked like more well-distributed in the hydrogels. However, the unique Pdots **2.5 PN** became uneven in size and agglomerated signals in the hydrogels. This result indicated that there is no significant change of Pdots signals in vitro and *in vivo*.

Furthermore, as shown in Fig. 5G, it showed that Pdots and LVs of the LN had the most signal coverage. In addition, in Figure S12 and 5H, the dense collagen fiber network of the LN was observed, and the yellow Pdots signals were existed in the connecting region, especially in the outer layer. As shown in Fig. 5I [28], only blue signals represented blood endothelial cells, purple signals that blue and red signals overlapped represented LECs, and red signals represented fibroblast reticular cells. Pdots signals were mainly retained in LVs and collagen fibers and rarely in blood vessels. These results suggested that LVs and collagen fibers are likely to provide a convenient channel for Pdots to transfer and react with immune cells in different sites of LNs.

4. Conclusion

In summary, we studied the relationship between Pdots and immune cells or channels in lymphatics. In the LV, Pdots existed in the extracellular of LECs, and last up to 21 d. In addition, Pdots image the whole LN with the aid of LVs, reticular network, and phagocytosis cells. This study provides an imaging-time window for Pdots to monitor the change both in the LNs and LVs. Furthermore, based on the property of Pdots phagocytosed by macrophages and monocytes, it can help to design imaging probes of carrying drugs or antigens for therapy. And functioned Pdots could effectively affect DCs to cause the immune response via collagen fibers, and microscopic imaging the process *in vivo*.

Credit author statement

Yufan Zhang: Conceptualization, Data curation, Formal analysis, Investigation, Methodology, Software, Validation, Visualization, Writing - original draft, Writing - review & editing. **Juxiang Zhang:** Investigation, Methodology, Visualization. **Xiaowei Li:** Methodology. **Jingru Li**: Formal analysis, Methodology. **Shuting Lu**: Validation. **Yuqiao Li**: Validation. **Panting Ren**: Visualization. **Chunfu Zhang:** Methodology. **Liqin Xiong:** Conceptualization, Data curation, Funding acquisition, Project administration, Resources, Supervision, Writing - review & editing.

Declaration of competing interest

The authors declare that they have no known competing financial interests or personal relationships that could have appeared to influence the work reported in this paper.

Acknowledgements

Thank for Shanghai Jiaotong University Instrumental Analysis Center to support advanced instruments such as super-resolution two-photon microscope and provide detailed technical guidance. This study was supported by grants from the National Natural Science Foundation of China (81974273, 81671738 and 81301261), and the Medical Engineering Cross Research Fund Project of Shanghai Jiao Tong University (YG2021QN31).

Appendix A. Supplementary data

Supplementary data to this article can be found online at https://doi.org/10.1016/j.mtbio.2022.100317.

References

[1] D. Hu, L. Li, S. Li, M. Wu, N. Ge, Y. Cui, Z. Lian, J. Song, H. Chen, Lymphatic system identification, pathophysiology and therapy in the cardiovascular diseases, J. Mol. Cell. Cardiol. 133 (2019) 99–111, https://doi.org/10.1016/j.yjmcc.2019.06.002.

[2] L. Xiong, H. Engel, E. Gazyakan, M. Rahimi, M. Hünerbein, J. Sun, U. Kneser, C. Hirche, Current techniques for lymphatic imaging: state of the art and future perspectives, Eur. J. Surg. Oncol. 40 (3) (2014) 270–276, https://doi.org/10.1016/j.ejso.2013.11.027.

[3] L.L. Munn, T.P. Padera, Imaging the lymphatic system, Microvasc. Res. 96 (2014) 55–63, https://doi.org/10.1016/j.mvr.2014.06.006.

[4] C. Chong, F. Scholkmann, S.B. Bachmann, P. Luciani, J.C. Leroux, M. Detmar, S.T. Proulx, In vivo visualization and quantification of collecting lymphatic vessel contractility using near-infrared imaging, Sci. Rep. 6 (2016), 22930, https://doi.org/10.1038/srep22930.

[5] P. Schineis, P. Runge, C. Halin, Cellular traffic through afferent lymphatic vessels, Vasc. Pharmacol. 112 (2019) 31–41, https://doi.org/10.1016/j.vph.2018.08.001.

[6] G.B. Chavhan, C.Z. Lam, M.L.C. Greer, M. Temple, J. Amaral, L. Grosse-Wortmann, Magnetic resonance lymphangiography, Radiol. Clin. 58 (4) (2020) 693–706, https://doi.org/10.1016/j.rcl.2020.02.002.

[7] N. Telinius, V.E. Hjortdal, Role of the lymphatic vasculature in cardiovascular medicine, Heart 105 (23) (2019) 1777–1784, https://doi.org/10.1136/heartjnl-2018-314461.
[8] A.K. Goswami, M.S. Khaja, T. Downing, N. Kokabi, W.E. Saad, B.S. Majdalany, Lymphatic anatomy and physiology, Semin. Intervent. Radiol. 37 (3) (2020) 227–236, https://doi.org/10.1055/s-0040-1713440.
[9] D. Olmeda, D. Cerezo-Wallis, E. Castellano-Sanz, S. García-Silva, H. Peinado, M.S. Soengas, Physiological models for in vivo imaging and targeting the lymphatic system: nanoparticles and extracellular vesicles, Adv. Drug Deliv. Rev. 175 (2021), 113833, https://doi.org/10.1016/j.addr.2021.113833.
[10] M. Ballard, K.T. Wolf, Z. Nepiyushchikh, J.B. Dixon, A. Alexeev, Probing the effect of morphology on lymphatic valve dynamic function, Biomech. Model. Mechanobiol. 17 (5) (2018) 1343–1356, https://doi.org/10.1007/s10237-018-1030-y.
[11] G. Pons, J.B. Tang, Major changes in lymphatic microsurgery and microvascular surgery in past 20 years, Clin. Plast. Surg. 47 (4) (2020) 679–683, https://doi.org/10.1016/j.cps.2020.07.004.
[12] A. Schudel, A.P. Chapman, M.K. Yau, C.J. Higginson, D.M. Francis, M.P. Manspeaker, A.R.C. Avecilla, N.A. Rohner, M.G. Finn, S.N. Thomas, Programmable multistage drug delivery to lymph nodes, Nat. Nanotechnol. 15 (6) (2020) 491–499, https://doi.org/10.1038/s41565-020-0679-4.
[13] M.C. Hunter, A. Teijeira, R. Montecchi, E. Russo, P. Runge, F. Kiefer, C. Halin, Dendritic cells and T cells interact within murine afferent lymphatic capillaries, Front. Immunol. 10 (2019) 520, https://doi.org/10.3389/fimmu.2019.00520.
[14] D. Olmeda, D. Cerezo-Wallis, E. Castellano-Sanz, S. García-Silva, H. Peinado, M.S. Soengas, Physiological models for in vivo imaging and targeting the lymphatic system: nanoparticles and extracellular vesicles, Adv. Drug Deliv. Rev. 175 (2021), 113833, https://doi.org/10.1016/j.addr.2021.113833.
[15] M.E.J. Stouthandel, L. Veldeman, T. Van Hoof, Call for a multidisciplinary effort to map the lymphatic system with advanced medical imaging techniques: a review of the literature and suggestions for future anatomical research, Anat. Rec. 302 (10) (2019) 1681–1695, https://doi.org/10.1002/ar.24143.
[16] A.K. Polomska, S.T. Proulx, Imaging technology of the lymphatic system, Adv. Drug Deliv. Rev. 170 (2021) 294–311, https://doi.org/10.1016/j.addr.2020.08.013.
[17] M.V. Novoselova, T.O. Abakumova, B.N. Khlebtsov, T.S. Zatsepin, E.N. Lazareva, V.V. Tuchin, V.P. Zharov, D.A. Gorin, E.I. Galanzha, Optical clearing for photoacoustic lympho- and angiography beyond conventional depth limit in vivo, Photoacoustics 20 (2020), 100186, https://doi.org/10.1016/j.pacs.2020.100186.
[18] Y. Guo, Y. Li, Y. Yang, S. Tang, Y. Zhang, L. Xiong, Multiscale imaging of Brown adipose tissue in living mice/rats with fluorescent polymer dots, ACS Appl. Mater. Interfaces 10 (24) (2018) 20884–20896, https://doi.org/10.1021/acsami.8b06094.
[19] Y. Li, Y. Yang, S. Tang, Y. Zhang, X. Li, W. Guan, F. Ma, C. Zhang, L. Xiong, High-resolution imaging of the lymphatic vascular system in living mice/rats using dual-modal polymer dots, ACS Appl. Bio Mater. 2 (9) (2019) 3877–3885, https://doi.org/10.1021/acsabm.9b00479.
[20] F. Cao, Y. Guo, Y. Li, S. Tang, Y. Yang, H. Yang, L. Xiong, Fast and accurate imaging of lymph node metastasis with multifunctional near-infrared polymer dots, Adv. Funct. Mater. 28 (16) (2018), 1707174, https://doi.org/10.1002/adfm.201707174.
[21] Y. Zhang, Y. Li, S. Tang, X. Li, W. Guan, X. Li, Y. Li, C. Zhang, L. Xiong, Modified polymer dots for multi-scale multi-modal imaging of lymphatic system in tumor pre-metastasis, Appl. Mater. Today 21 (2020), 100863, https://doi.org/10.1016/j.apmt.2020.100863.
[22] B. Jeremiasse, C.H. van den Bosch, M.W.H.A. Wijnen, C.E.J. Terwisscha van Scheltinga, M.F. Fiocco, A.F.W. van der Steeg, Systematic review and meta-analysis concerning near-infrared imaging with fluorescent agents to identify the sentinel lymph node in oncology patients, Eur. J. Surg. Oncol. 46 (11) (2020) 2011–2022, https://doi.org/10.1016/j.ejso.2020.07.012.
[23] Y. Zhang, Y. Li, Y. Guo, Y. Yang, S. Tang, L. Xiong, Fluorescent polymer dots for tracking SKOV3 cells in living mice with probe-based confocal laser endomicroscopy, Mol. Imag. Biol. 21 (6) (2019) 1026–1033, https://doi.org/10.1007/s11307-019-01343-4.
[24] C. Pan, R. Cai, F.P. Quacquarelli, A. Ghasemigharagoz, A. Lourbopoulos, P. Matryba, N. Plesnila, M. Dichgans, F. Hellal, A. Ertürk, Shrinkage-mediated imaging of entire organs and organisms using UDISCO, Nat. Methods 13 (10) (2016) 859–867, https://doi.org/10.1038/nmeth.3964.
[25] L.F. Sestito, S.N. Thomas, Lymph-directed nitric Oxide increases immune cell access to lymph-borne nanoscale solutes, Biomaterials 265 (2021), 120411, https://doi.org/10.1016/j.biomaterials.2020.120411.
[26] P. Matryba, A. Sosnowska, A. Wolny, L. Bozycki, A. Greig, J. Grzybowski, M. Stefaniuk, D. Nowis, J. Gołąb, Systematic evaluation of chemically distinct tissue optical clearing techniques in murine lymph nodes, J. Immunol. 204 (5) (2020) 1395–1407, https://doi.org/10.4049/jimmunol.1900847.
[27] K.A. Kang, C. Maldonado, V. Vodyanoy, Technical challenges in current primo vascular system research and potential solutions, J. Acupunct. Meridian 9 (6) (2016) 297–306, https://doi.org/10.1016/j.jams.2016.02.001.
[28] V. Saxena, L. Li, C. Paluskievicz, V. Kasinath, A. Bean, R. Abdi, C.M. Jewell, J.S. Bromberg, Role of lymph node stroma and microenvironment in T cell tolerance, Immunol. Rev. 292 (1) (2019) 9–23, https://doi.org/10.1111/imr.12799.